Acta Crystallographica Section B
Structural Science
ISSN 0108-7681

Temperature-dependent analysis of thermal motion, disorder and structures of tris(ethylenediamine)-zinc(II) sulfate and tris(ethylenediamine)copper(II) sulfate

Stef Smeets,[a] Pascal Parois,[a] Hans-Beat Bürgi[b,c] and Martin Lutz[a]*

[a]Bijvoet Center for Biomolecular Research, Crystal and Structural Chemistry, Faculty of Science, Utrecht University, Padualaan 8, 3584 CH Utrecht, The Netherlands, [b]Laboratory for Chemical and Mineralogical Crystallography, University of Berne, Freiestrasse 3, CH-3012 Berne, Switzerland, and [c]Institute of Organic Chemistry, University of Zürich, Winterthurerstrasse 190, CH-8057 Zürich, Switzerland

Correspondence e-mail: m.lutz@uu.nl

Received 22 October 2010
Accepted 28 December 2010

The crystal structures of the title compounds have been determined in the temperature range 140–290 K for the zinc complex, and 190–270 K for the copper complex. The two structures are isostructural in the trigonal space group $P\bar{3}1c$ with the sulfate anion severely disordered on a site with 32 (D_3) symmetry. This sulfate disorder leads to a disordered three-dimensional hydrogen-bond network, with the N—H atoms acting as donors and the sulfate O atoms as acceptors. The displacement parameters of the N and C atoms in both compounds contain disorder contributions in the out-of-ligand plane direction owing to ring puckering and/or disorder in hydrogen bonding. In the Zn compound the vibrational amplitudes in the bond directions are closely similar. Their differences show no significant deviations from rigid-bond behaviour. In the Cu compound, a (presumably) dynamic Jahn–Teller effect is identified from a temperature-independent contribution to the displacement ellipsoids of the N atom along the N—Cu bond. These conclusions derive from analyses of the atomic displacement parameters with the Hirshfeld test, with rigid-body models at different temperatures, and with a normal coordinate analysis. This analysis considers the atomic displacement parameters (ADPs) from all different temperatures simultaneously and provides a detailed description of both the thermal motion and the disorder in the cation. The Jahn–Teller radii of the Cu compound derived on the basis of the ADP analysis and from the bond distances in the statically distorted low-temperature phase [Lutz (2010). *Acta Cryst.* C**66**, m330–m335] are found to be the same.

1. Introduction

The crystal structures of $Cu^{II}N_6$ complexes sometimes show six equal Cu—N distances in apparent violation of the Jahn–Teller theorem which predicts such complexes to be distorted, mostly tetragonally elongated. However, whenever the crystal structure suggests equal Cu—N bonds, the anisotropic displacement parameters (ADPs) have been shown to be unusual. Such ADPs have previously been studied with a semi-rigid body model by analyzing differences in mean-square displacement amplitudes along Cu—N bonds or with a model of dynamic, Jahn–Teller coupling (Ammeter *et al.*, 1979; Falvello, 1997; Halcrow, 2003).

In this paper the structures of tris(ethylenediamine)zinc(II) sulfate (1) and tris(ethylenediamine)copper(II) sulfate (2) are determined over the temperature ranges 150 (1) and 80 K (2). The ADPs and their temperature dependence are analyzed using rigid-body analysis for each temperature separately (Schomaker & Trueblood, 1998) and normal coordinate analysis, which considers the ADPs from all temperatures

Table 1
Experimental details of (1) and (2).

For all structures: trigonal, $P\bar{3}1c$, Z = 2. Experiments were carried out with Mo $K\alpha$ radiation using a Nonius KappaCCD diffractometer. Analytical, *SADABS*2008/1 (Sheldrick, 2008*b*). Refinement was on 49 parameters with 16 restraints. H atoms were treated with a mixture of independent and constrained refinement.

	(1*a*)	(1*b*)	(1*c*)	(1*d*)	(1*e*)	(1*f*)
Crystal data						
Chemical formula	$[Zn(C_6H_{24}N_6)]^{2+}SO_4^{2-}$	$[Zn(C_6H_{24}N_6)]^{2+}SO_4^{2-}$	$[Zn(C_6H_{24}N_6)]^{2+}SO_4^{2-}$	$[Zn(C_6H_{24}N_6)]^{2+}SO_4^{2-}$	$[Zn(C_6H_{24}N_6)]^{2+}SO_4^{2-}$	$[Zn(C_6H_{24}N_6)]^{2+}SO_4^{2-}$
M_r	341.13	341.13	341.13	341.13	341.13	341.13
Temperature (K)	140	170	200	230	260	290
a, c (Å)	8.9594 (1), 9.5583 (1)	8.9649 (1), 9.5685 (1)	8.9696 (2), 9.5842 (1)	8.9790 (1), 9.5973 (2)	8.9855 (2), 9.6043 (1)	8.9929 (2), 9.6101 (2)
V (Å 3)	664.46 (2)	665.99 (2)	667.78 (3)	670.09 (2)	671.55 (3)	673.07 (2)
μ (mm^{-1})	2.02	2.02	2.01	2.01	2.00	2.00
Crystal size (mm)	0.30 × 0.09 × 0.09	0.30 × 0.09 × 0.09	0.30 × 0.09 × 0.09	0.30 × 0.09 × 0.09	0.30 × 0.09 × 0.09	0.30 × 0.09 × 0.09
Data collection						
T_{min}, T_{max}	0.619, 0.878	0.625, 0.876	0.622, 0.882	0.625, 0.878	0.621, 0.874	0.627, 0.872
No. of measured, independent and observed [$I > 2\sigma(I)$] reflections	10 729, 683, 649	10 818, 689, 650	10 832, 690, 652	10 896, 694, 649	11 110, 694, 653	11 155, 696, 647
R_{int}	0.027	0.026	0.027	0.027	0.029	0.030
Refinement						
$R[F^2 > 2\sigma(F^2)]$, $wR(F^2)$, S	0.020, 0.048, 1.10	0.021, 0.051, 1.07	0.022, 0.058, 1.05	0.023, 0.061, 1.08	0.024, 0.063, 1.05	0.023, 0.064, 1.06
No. of reflections	683	689	690	694	694	696
$\Delta\rho_{max}$, $\Delta\rho_{min}$ (e Å^{-3})	0.56, −0,25	0.53, −0.26	0.56, −0.25	0.59, −0.24	0.66, −0.29	0.62, −0.29

	(2*a*)	(2*b*)	(2*c*)	(2*d*)	(2*e*)
Crystal data					
Chemical formula	$[Cu(C_6H_{24}N_6)]^{2+}SO_4^{2-}$	$[Cu(C_6H_{24}N_6)]^{2+}SO_4^{2-}$	$[Cu(C_6H_{24}N_6)]^{2+}SO_4^{2-}$	$[Cu(C_6H_{24}N_6)]^{2+}SO_4^{2-}$	$[Cu(C_6H_{24}N_6)]^{2+}SO_4^{2-}$
M_r	339.91	339.91	339.91	339.91	339.91
Temperature (K)	190	210	230	250	270
a, c (Å)	8.9387 (1), 9.5766 (1)	8.9445 (1), 9.5826 (1)	8.9513 (1), 9.5876 (1)	8.9572 (1), 9.5926 (1)	8.9664 (1), 9.5996 (1)
V (Å^3)	662.66 (2)	663.94 (2)	665.29 (2)	666.52 (2)	668.38 (2)
μ (mm^{-1})	1.82	1.82	1.82	1.81	1.81
Crystal size (mm)	0.06 × 0.15 × 0.33	0.06 × 0.15 × 0.33	0.06 × 0.15 × 0.33	0.06 × 0.15 × 0.33	0.06 × 0.15 × 0.33
Data collection					
T_{min}, T_{max}	0.580, 0.940	0.581, 0.940	0.578, 0.937	0.579, 0.947	0.578, 0.947
No. of measured, independent and observed [$I > 2\sigma(I)$] reflections	9708, 683, 644	9739, 685, 637	9736, 687, 642	9785, 687, 638	9819, 690, 639
R_{int}	0.025	0.026	0.027	0.027	0.027
Refinement					
$R[F^2 > 2\sigma(F^2)]$, $wR(F^2)$, S	0.022, 0.056, 1.11	0.022, 0.057, 1.09	0.023, 0.060, 1.12	0.024, 0.061, 1.10	0.025, 0.065, 1.12
No. of reflections	683	685	687	687	690
$\Delta\rho_{max}$, $\Delta\rho_{min}$ (e Å^{-3})	0.45, −0.28	0.46, −0.26	0.51, −0.28	0.52, −0.29	0.56, −0.35

Computer programs used: *COLLECT* (Nonius, 1999), *PEAKREF* (Schreurs, 2005), *EVAL*15 (Schreurs *et al.*, 2010), *SADABS*2008/1 (Sheldrick, 2008*b*), *SHELXL*97, *SHELXS*97 (Sheldrick, 2008*a*).

simultaneously (Bürgi & Capelli, 2000). The normal coordinate algorithm aims to deconvolute the temperature-dependent thermal motion from the temperature-independent contributions to the ADPs.

The crystal structure of (1) was first determined by Neverov *et al.* (1990). It was found to crystallize in the trigonal space group $P\bar{3}1c$. The crystal structure of (1) is isostructural with that of (2), which was first determined by Cola *et al.* (1962) and then redetermined by Cullen & Lingafelter (1970) and Bertini *et al.* (1979).

2. Experimental

Compounds (1) and (2) were prepared at room temperature by slowly adding excess ethylenediamine to a solution of the

Table 2
Hydrogen-bond geometry (Å, °) for (1) from 140 to 290 K and (2) from 190 to 270 K.

T (K)	D—H···A	D—H	H···A	D···A	D—H···A
(1)					
140	N1—H1N···O1	0.84 (2)	1.97 (2)	2.799 (3)	170 (2)
170	N1—H1N···O1	0.83 (2)	1.99 (2)	2.810 (4)	169 (2)
200	N1—H1N···O1	0.86 (3)	1.97 (3)	2.823 (5)	170 (2)
230	N1—H1N···O1	0.87 (3)	1.98 (3)	2.835 (5)	169 (2)
260	N1—H1N···O1	0.86 (3)	1.99 (3)	2.839 (5)	172 (3)
290	N1—H1N···O1	0.86 (3)	1.99 (3)	2.846 (6)	172 (3)
140	N1—H2N···O2^{i}	0.84 (2)	2.12 (2)	2.951 (4)	178 (2)
170	N1—H2N···O2^{i}	0.85 (2)	2.11 (2)	2.966 (5)	177 (2)
200	N1—H2N···O2^{i}	0.86 (2)	2.15 (2)	3.006 (5)	177 (2)
230	N1—H2N···O2^{i}	0.84 (2)	2.18 (2)	3.019 (6)	177 (2)
260	N1—H2N···O2^{i}	0.87 (2)	2.16 (2)	3.022 (6)	177 (2)
290	N1—H2N···O2^{i}	0.86 (2)	2.17 (2)	3.029 (6)	178 (2)
(2)					
190	N1—H1N···O1	0.81 (3)	2.01 (3)	2.816 (5)	172 (2)
210	N1—H1N···O1	0.81 (3)	2.01 (3)	2.821 (5)	172 (2)
230	N1—H1N···O1	0.80 (3)	2.03 (3)	2.825 (6)	172 (3)
250	N1—H1N···O1	0.81 (3)	2.02 (3)	2.827 (6)	173 (3)
270	N1—H1N···O1	0.82 (3)	2.01 (3)	2.832 (6)	175 (3)
190	N1—H2N···O2^{i}	0.83 (2)	2.19 (2)	3.017 (6)	179 (2)
210	N1—H2N···O2^{i}	0.83 (2)	2.19 (2)	3.017 (6)	179 (2)
230	N1—H2N···O2^{i}	0.83 (2)	2.20 (3)	3.022 (6)	179 (2)
250	N1—H2N···O2^{i}	0.83 (3)	2.19 (3)	3.022 (7)	180 (3)
270	N1—H2N···O2^{i}	0.84 (3)	2.19 (3)	3.025 (7)	180 (3)

Symmetry code: (i) $x-y, x, -z$.

corresponding metal salt in water. Single crystals were obtained by evaporating the solutions at room temperature.

Diffraction data were collected from single crystals of (1) and (2) on a Nonius KappaCCD diffractometer with rotating anode and graphite-monochromated Mo $K\alpha$ radiation (λ = 0.71073 Å) up to θ_{max} = 30.5°. The measurement temperatures were 140, 170, 200, 230, 260 and 290 K for (1), and 190, 210, 230, 250 and 270 K for (2). Data taken at temperatures lower than 140 and 190 K are not discussed here since both (1) and (2) undergo phase transitions on cooling. The temperatures were chosen in order to obtain a similar number of measurement points for both structures. Data were collected using the program *COLLECT* (Nonius, 1999) and integrated with *EVAL*15 (Schreurs *et al.*, 2010). Cell refinement was done using *PEAKREF* (Schreurs, 2005), and absorption correction and scaling were performed with *SADABS* (Sheldrick, 2008*b*). Structure refinement was carried out with *SHELXL*97 (Sheldrick, 2008*a*) against $|F|^2$ using all data. Crystal structures were visualized using *PLATON* (Spek, 2009) and *Jmol* (Hanson, 2010). Amine H atoms, H1N and H2N, were found in difference-Fourier maps and refined freely with isotropic displacement parameters. Ethylene H atoms, H1*A* and H1*B*, were refined with a riding model. Experimental details are summarized in Table 1.

The S atom is located on a site with 32 (D_3) symmetry, incompatible with the symmetry $\bar{4}3m$ (T_d) of the sulfate ion. Therefore, we chose a disorder model based on two crystal-

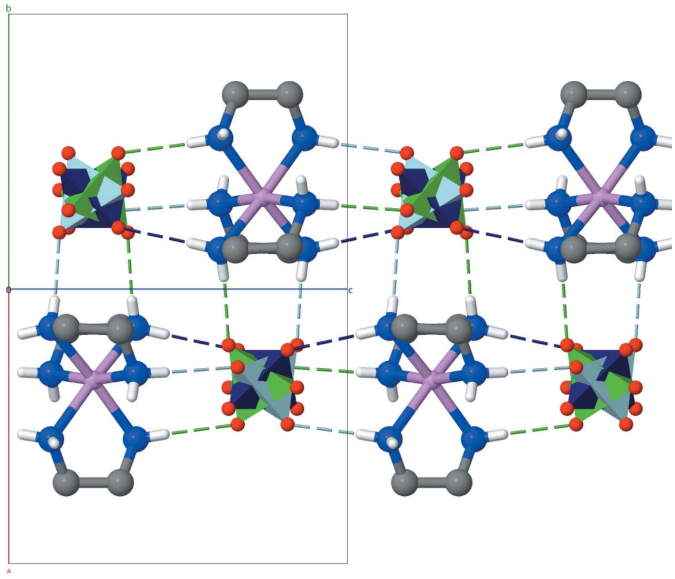

Figure 1
Schematic representation of the hydrogen bonding in (1) and (2). Each of the three disordered tetrahedra is represented by a different colour. Associated hydrogen bonds are coloured correspondingly. View along [110].

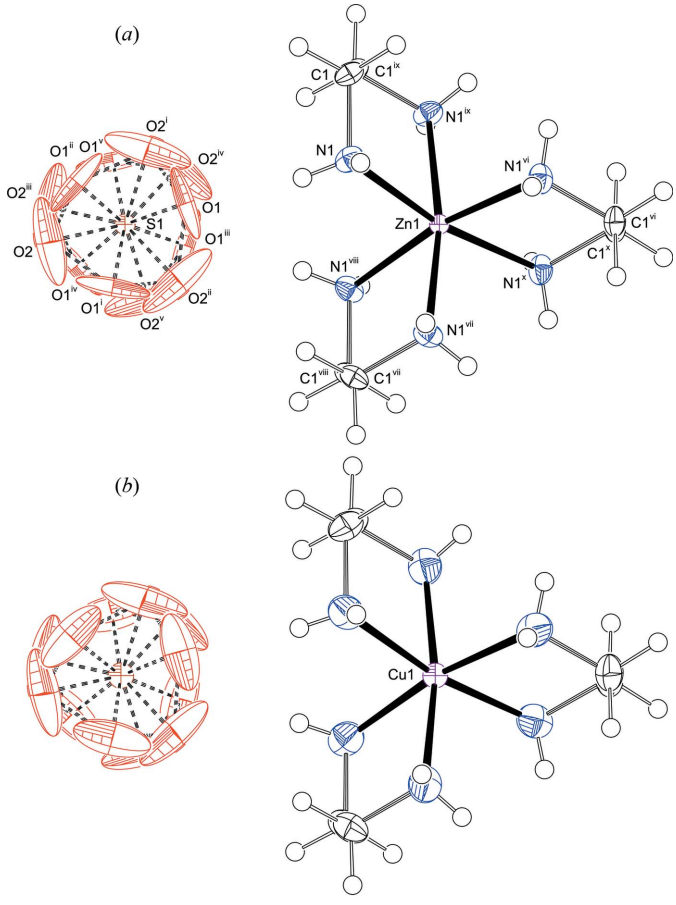

Figure 2
Displacement ellipsoid plot and labeling scheme of (*a*) (1) at 140 K and (*b*) (2) at 190 K drawn at the 50% probability level. The labeling scheme is the same for both figures. Symmetry codes: (i) $1-y, 1+x-y, z$; (ii) $-x+y, 1-x, z$; (iii) $1-y, 1-x, \frac{1}{2}-z$; (iv) $x, 1+x-y, \frac{1}{2}-z$; (v) $-x+y, y, \frac{1}{2}-z$; (vi) $1-y, x-y, z$; (vii) $1-x+y, 1-x, z$; (viii) $1-y, 1-x, \frac{1}{2}-z$; (ix) $x, x-y, \frac{1}{2}-z$; (x) $1-x+y, y, \frac{1}{2}-z$.

Table 3
Selected bonds lengths (Å), angles and torsion angles (°) of (1) and (2) (M = Zn, Cu).

	(1)		(2)	
T (K)	140	290	190	270
M1—N1	2.1832 (13)	2.1866 (16)	2.1473 (18)	2.1495 (19)
N1—C1	1.4720 (19)	1.469 (2)	1.473 (2)	1.474 (2)
C1—C1^{i}	1.5213 (18)	1.513 (2)	1.514 (2)	1.511 (2)
N1—M1—N1^{ii}	170.26 (4)	170.09 (6)	170.97 (6)	170.95 (6)
N1—M1—N1^{iii}	92.93 (5)	93.02 (6)	92.83 (7)	92.85 (7)
N1—M1—N1^{iv}	94.50 (5)	94.56 (6)	94.04 (6)	94.03 (7)
N1—M1—N1^{i}	80.43 (5)	80.21 (6)	80.99 (6)	80.95 (7)
N1—C1—C1^{i}	108.99 (11)	109.14 (15)	108.40 (14)	108.50 (15)
M1—N1—C1	107.93 (9)	107.81 (11)	108.09 (11)	108.03 (12)
N1—C1—C1^{i}—N1^{i}	−57.66 (16)	−57.9 (2)	−57.4 (2)	−57.5 (2)

Symmetry codes: (i) $x, x-y, \frac{1}{2}-z$; (ii) $1-x+y, y, \frac{1}{2}-z$; (iii) $1-y, x-y, z$; (iv) $1-x, 1-y, \frac{1}{2}-z$.

lographically independent O atoms resulting in three interpenetrating tetrahedra. The first tetrahedron is described by the independent O atoms and the symmetry operation $-x+y, y, -z+\frac{1}{2}$; the second tetrahedron uses symmetry operations $x, x-y+1, -z+\frac{1}{2}$ and $-x+y, 1-x, z$; the third is based on symmetry operations $-y+1, x-y+1, z$ and $1-y, 1-x, -z+\frac{1}{2}$ (Figs. 1 and 2).

3. Crystal and molecular structures

The crystal structures of (1) and (2) are isomorphous over the common temperature range 190–270 K, as are the structures of the corresponding Co (Yotnoi *et al.*, 2010), Ni (Caughlan *et al.*, 1970) and V complexes (Daniels *et al.*, 1995). The unit cell consists of two tris(en)M^{II} (en = ethylenediamine) cations and two disordered sulfate anions. The cations and anions alternate in rows along the c axis (Fig. 1). Each of the three disordered sulfate ions forms four nearly linear hydrogen bonds with amine protons of the cations, one per partially occupied O atom. The sulfate accepts hydrogen bonds of two types: one from an H2N of the cation immediately above and below, as well as one from an H1N of the three cations surrounding it (atomic numbering in Fig. 2). The stronger hydrogen bond is between N1—H1N and O1; it is nearly perpendicular to the threefold axis of the space group. The hydrogen bond between N1—H2N and O2^{i} [(i) $x-y, x, -z$] is approximately parallel to the threefold axis (Table 2). On average, each of the 12 amine protons of the cation forms a hydrogen bond with the probability $\frac{1}{3}$ to one of three disordered sulfate ions. Every cation is thus involved in only four hydrogen bonds. Its hydrogen-bond arrangement depends on the actual orientation of the five surrounding sulfate ions and will not satisfy the average crystallographic symmetry 32 (D_3). The hydrogen-bonding pattern might be responsible for some orientational disorder of the cations (see §4). Overall, the hydrogen bonds form a three-dimensional network. There is only a small variation of the hydrogen-bond geometry over the observed temperature range, just enough to account for the observed decrease in cell parameters with decreasing temperature. Measurements of (1) below 140 K and of (2) below 190 K were not considered in the present study, owing to the solid–solid phase transitions accompanied by space-group changes from $P\bar{3}1c$ to $P\bar{3}$ for (1) and to $P\bar{1}$ for (2) (Lutz, 2010). In the ordered low-temperature phases the $[Zn(en)_3]^{2+}$ cation forms 12 hydrogen bonds and the $[Cu(en)_3]^{2+}$ cation 13, of which one is bifurcated.

Thermal expansion does not affect the intramolecular geometries in the observed temperature ranges; all values are equal to each other within 3σ (Table 3). The N—M—N bite angles of the en ligands are $\sim 80°$, significantly smaller than the ideal octahedral angle of 90°. Consequently, the other angles at the metal also deviate from 90°. The M—N—C and N—C—C angles are close to the expected 109° value. The five-membered chelate ring is non-planar and – owing to space-group symmetry – in an exact C_2 symmetric half-chair conformation. The N—C—C—N torsion angle is close to 60° (Table 3).

4. Disorder and thermal motion

In contrast to the intra- and intermolecular geometries, atomic displacement parameters (ADPs, historically known as temperature factor parameters) are expected to change with temperature. These changes will be explored in three steps: first the temperature dependence of the ADPs of individual atoms will be analyzed; second rigid-body models will be tested, one per temperature, for their potential to explain the ADPs of an entire cation; third a single normal mode analysis will be performed for each complex based on all ADPs over the full temperature ranges investigated. In the following only the cationic metal complexes are considered because of the severe orientational disorder of the sulfate anion.

4.1. Temperature dependence of the atomic displacement parameters

For harmonic thermal motion in the classical regime, a plot of the equivalent isotropic ADPs *versus* temperature is expected to show a linear relationship that extrapolates to an intercept of 0 at $T = 0$ K. Such plots for (1) and (2) are indeed linear (see Figs. S1 and S2 in the supplementary material[1]). However, for the C and especially the N atoms, the intercept at $T = 0$ K deviates significantly from 0. For an explanation of this anomaly the anisotropic ADPs were analyzed.

The three eigenvalues of the ADPs of the N atoms are plotted *versus* temperature in Fig. 3. As for the isotropic ADPs, a linear dependence on temperature extrapolating to an intercept of 0 at $T = 0$ K is expected. Such behaviour is followed reasonably well for all three eigenvalues of the M and C atoms and the two smaller eigenvalues λ_2 and λ_3 of the N atom. However, linear regression of the largest eigenvalue λ_1 of the N atom in (1) reveals an intercept of 0.0176 (9) Å^2, significantly different from 0. This indicates a significant,

[1] Supplementary data for this paper are available from the IUCr electronic archives (Reference: BK5101). Services for accessing these data are described at the back of the journal.

temperature-independent contribution to the ADPs which is not due to thermal motion. For (2) the intercepts, and thus the temperature-independent contributions, are even larger, with 0.03071 (12) Å^2 for λ_1 and 0.0126 (12) Å^2 and 0.00666 (9) Å^2 for λ_2 and λ_3.

These results have been tested for the influence of experimental resolution by lowering θ_{max} from 30.5 to 22° (see Fig. S3 of the supplementary material). The eigenvalues λ_1 of N in (1) found with the low-resolution data extrapolate to an intercept of 0.0132 (11) Å^2, lower than the value of 0.0176 (9) Å^2 found with the full data, but still higher than the corresponding intercepts for λ_2 and λ_3: 0.0050 (6) and 0.0039 (8) Å^2. The indication for a temperature-independent contribution to the ADPs is thus still present, if less significant. The difference may be attributed to the fact that for low-resolution data ADPs are more influenced by the non-spherical valence electron density than for high-resolution data (Dittrich *et al.*, 2008). Temperature-independent contributions of this magnitude are usually associated with unresolved positional disorder of the affected atoms (Bürgi & Capelli, 2003), as will be discussed in more detail in §§4.2 and 4.3.

The quality of the ADPs has also been assessed with Hirshfeld tests (Hirshfeld, 1976). The temperature-averaged, absolute differences of the ADPs along the C—N directions are 0.0005 and 0.0010 Å^2 for (1) and (2). These are within the limit of 0.0010 Å^2 suggested by Hirshfeld for rigid bonds. The differences along the C—C bonds are zero owing to the twofold symmetry relating the two atoms. The corresponding temperature-averaged differences $\langle U_z(\mathrm{N}) - U_z(M)\rangle_T$ are 0.0017 and 0.0269 Å^2 for (1) and (2). The former value is typical for stretching vibrations of NiN_6 or ZnN_6 complexes (*e.g.* the NiN_6 structure in Ammeter *et al.*, 1979); the latter value is typical of crystal structures with apparently undistorted Cu^{II}—N_6 complexes (Ammeter *et al.*, 1979). It indicates an average structure that is a superposition of three Jahn–Teller distorted octahedral complexes, each elongated along a different octahedral axis.

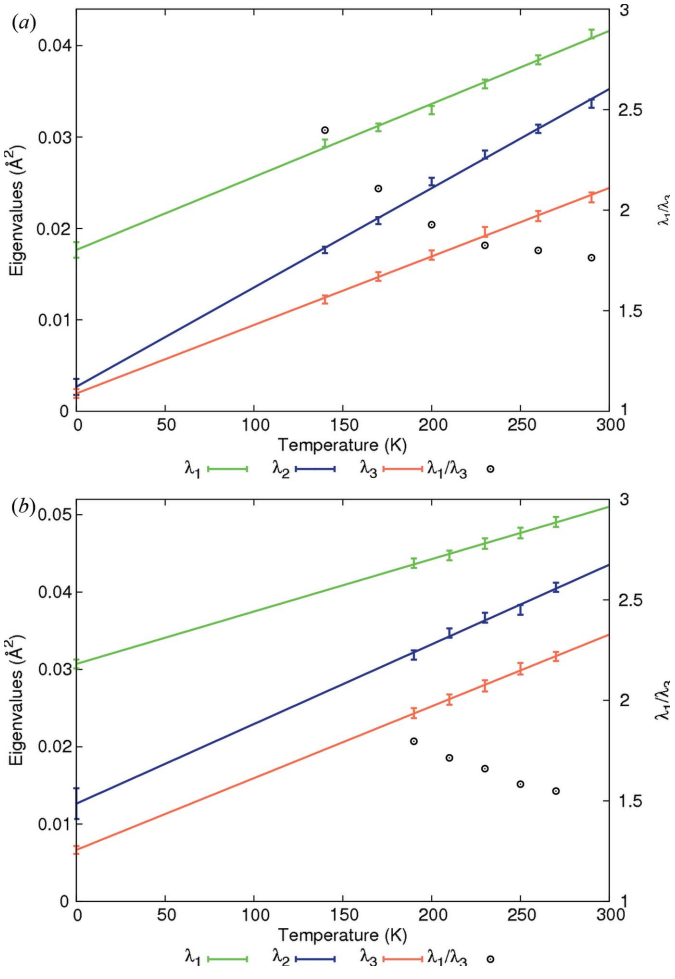

Figure 3
Temperature evolution of the eigenvalues λ and their ratios (λ_1/λ_3) of the ADPs of the N atom for (*a*) (1) and (*b*) (2). For (1) λ_1 has a slope of 8.0 (4) × 10^{-5} Å^2 K^{-1} and an intercept of 0.0176 (9) Å^2 at T = 0 K, λ_2 has 10.9 (4) × 10^{-5} Å^2 K^{-1} and 0.0027 (9) Å^2 and λ_3 has 7.5 (2) × 10^{-5} Å^2 K^{-1} and 0.0019 (5) Å^2; corresponding values for (2) are: for λ_1 6.78 (6) × 10^{-5} Å^2 K^{-1} and 0.03071 (12) Å^2, for λ_2 10.3 (5) × 10^{-5} Å^2 K^{-1} and 0.0126 (12) Å^2 and for λ_3 9.28 (5) × 10^{-5} Å^2 K^{-1} and 0.00666 (9) Å^2. Standard uncertainties for the eigenvalues were calculated using a locally written routine (Parois, 2010).

4.2. Rigid-body analyses

Rigid-body analyses were performed on the atomic displacement parameters (ADPs) of (1) and (2) at each temperature using *THMA*11 (Schomaker & Trueblood, 1998). In the TLS analysis of (1) and (2), the smallest T tensor component is T_3, oriented along the threefold rotation axis; the larger, degenerate components T_1 and T_2 are perpendicular to this axis in the *ab* plane. For the L tensor the largest tensor component L_1 describes libration about the threefold axis, and L_2 and L_3 are again degenerate in the plane perpendicular to this axis. In both (1) and (2) the T and L tensors are approximately isotropic with maximum ratios L_1/L_3 = 1.29 for (1) and T_1/T_3 =

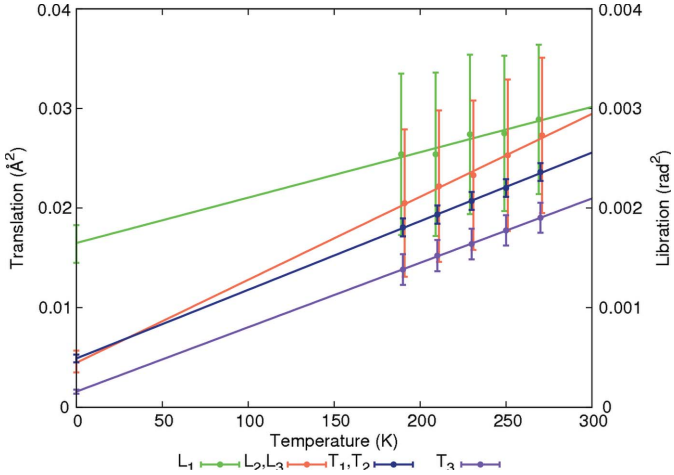

Figure 4
Temperature evolution of the eigenvalues of the translation (left axis, Å^2) and libration (right axis, rad^2) tensors for (2), as calculated with *THMA*11 (Schomaker & Trueblood, 1998). At T = 0 K the standard uncertainties of the intercepts of the four interpolations are drawn. A corresponding plot for (1) can be found in Fig. S4 of the supplementary material.

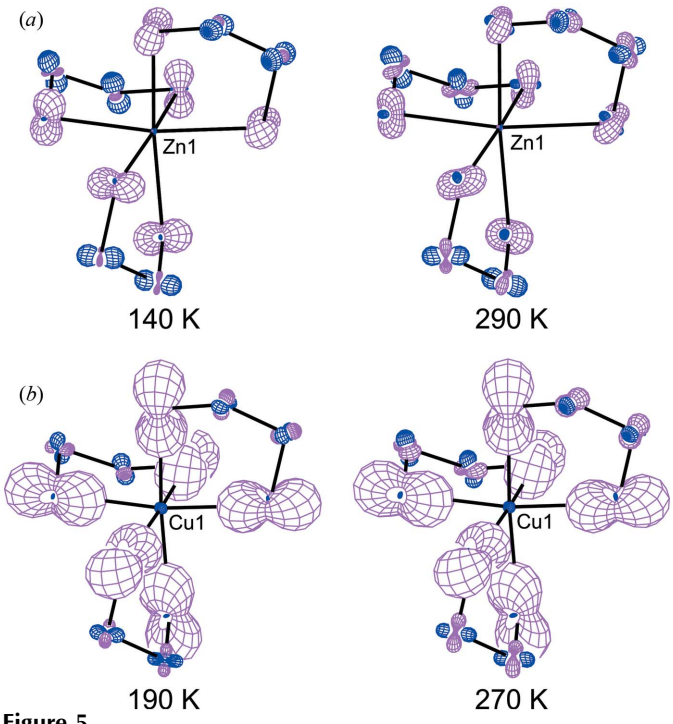

Figure 5
PEANUT plots $(U_{obs} - U_{calc})^{1/2} \times$ scale (Hummel *et al.*, 1990) of (*a*) (1) at 140 and 290 K, and (*b*) (2) at 190 and 270 K. The plots show the difference between the observed ADPs and those calculated from a TLS model with *THMA*11 (Schomaker & Trueblood, 1998). Scale is 6.15, light gray lines (red in the electronic online version) indicate positive differences, dark gray lines (blue in the online version) negative differences.

1.31 for (2). The elements of the screw-coupling tensors S equal zero within standard deviations (for the results of the rigid-body analyses, see Tables S1 and S2 of the supplementary material). The weighted R values[2] of the rigid-body model for (1), ranging from 0.110 to 0.047, indicate that this model is able to parameterize the ADPs at a given temperature fairly well. The weighted R values for TLS models of (2) are rather higher, ranging from 0.164 to 0.124.

A plot of the eigenvalues of the T and L tensors of (2) against temperature indicates significant temperature-independent contributions (Fig. 4). As in the case of the ADPs themselves (§4.1), these eigenvalues do not extrapolate to 0 at $T = 0$ K, with the possible exception of T_3. This finding implies that the rigid-body model absorbs not only contributions from librational and translational thermal motion, but also of orientational and positional disorder.

PEANUT plots (Hummel *et al.*, 1990) show the difference between the observed ADPs and those calculated from the rigid-body model, *i.e.* those contributions to the ADPs that cannot be represented as librational or translational displacements. Such differences are commonly displayed as surfaces representing $(U_{obs} - U_{calc})^{1/2}$. Fig. 5 shows such plots for (1) and (2) at two temperatures. The positive residual in the out-of-ligand plane direction for the N atom of (1) reflects disorder that is probably due to puckering of the saturated five-membered chelate ring and/or the disorder in hydrogen bonding (see §3). A TLS analysis of the room-temperature data for the isostructural Co complex reported by Yotnoi *et al.* (2010) reveals residual ADPs similar to those in (1).

PEANUT plots of (2) show large residual ADPs, primarily along the N—Cu directions as expected from the Hirshfeld tests (see §4.1). Fig. 5 nicely illustrates an interpretation of these residuals in terms of Jahn–Teller distortion: if two N atoms in a *trans* arrangement are placed into the outer lobes of the nitrogen peanuts and the other four into inner lobes, a tetragonal distortion is simulated. Although smaller, there are also positive differences in the out-of-ligand plane direction for the N atom as in (1). Since (1) and (2) are isostructural, these differences may be similarly assigned to puckering and/or to the disorder in hydrogen bonding. As in (1) there are only small differences between the *PEANUT* plots at different temperatures.

Table 4
Normal mode frequencies $\tilde{\nu}$ (cm^{-1}) and corresponding normalized eigenvectors (dimensionless) derived from ADPs at 140, 170, 200, 230, 260 and 290 K for (1), and at 190, 210, 230, 250 and 270 K for (2).

For the corresponding TLS tensors, see Tables S3 and S4 in the supplementary material.

$\tilde{\nu}$	70.1 (14)	70.1 (14)	62 (5)	35.4 (2)	35.4 (2)	34.3 (8)
(1)						
L_x	1	0	0	−0.00 (10)	0	0
L_y	0	1	0	0	−0.00 (9)	0
L_z	0	0	−0.96 (3)	0	0	−0.28 (9)
T_x	0.00 (9)	0	0	1	0	0
T_y	0	0.00 (9)	0	0	1	0
T_z	0	0	0.28 (9)	0	0	−0.96 (3)

$\tilde{\nu}$	61.2 (11)	61.2 (11)	67 (3)	36.9 (2)	36.9 (2)	39.3 (4)
(2)						
L_x	1	0	0	0.00 (11)	0	0
L_y	0	1	0	0	0.00 (11)	0
L_z	0	0	1	0	0	−0.00 (15)
T_x	0.00 (11)	0	0	1	0	0
T_y	0	0.00 (11)	0	0	1	0
T_z	0	0	0.00 (15)	0	0	1

4.3. Normal coordinate analysis

A simultaneous analysis of the ADPs from all temperatures was performed for (1) and (2) with the program *NKA* (Bürgi & Capelli, 2000; Capelli *et al.*, 2000). The aim of this analysis was to distinguish between thermal motion and disorder and thereby to obtain insight into the Jahn–Teller distortion by comparing the Jahn–Teller-active Cu^{II} compound with the Jahn–Teller inactive Zn^{II} compound. NKA separates multi-temperature ADPs into three contributions:

(i) those from temperature-dependent low-frequency normal modes (molecular libration and translation; soft intramolecular deformations, like torsions and out-of-plane motions),

(ii) contributions from temperature-independent high-frequency normal modes, and

[2] $R = [\sum(wU_{obs} - wU_{calc})^2 / \sum(wU_{obs})^2]^{1/2}$ with $w = \langle\sigma\rangle/\sigma$.

Table 5
ε tensor components and eigenvalues (Å^2) for (1) and (2).

Standard uncertainties of the eigenvalues were calculated using a locally written routine (Parois, 2010)

	Components						Eigenvalues		
	ε_{11}	ε_{22}	ε_{33}	ε_{12}	ε_{13}	ε_{23}	λ_1	λ_2	λ_3
(1)									
ε(Zn)	0.0005 (2)	0.0005 (2)	−0.0002 (2)	0	0	0	0.00052 (16)	0.00052 (16)	−0.0002 (2)
ε(N)	0.0021 (2)	0.0002 (3)	0.0135 (3)	−0.0029 (1)	−0.0005 (1)	0.0010 (2)	−0.0019 (3)	0.00406 (18)	0.0137 (3)
ε(C)	0.0036 (2)	0.0012 (3)	0.0066 (4)	−0.0002 (2)	−0.0013 (2)	−0.0028 (3)	0.0081 (5)	0.0035 (3)	−0.0001 (2)
(2)									
ε(Cu)	0.0041 (2)	0.0041 (2)	0.0016 (3)	0	0	0	0.00408 (19)	0.00407 (19)	0.0016 (3)
ε(N)	0.0302 (2)	0.0058 (3)	0.0117 (3)	−0.0009 (2)	−0.0012 (2)	0.0037 (2)	0.03038 (18)	0.0133 (3)	0.0040 (3)
ε(C)	0.0101 (3)	0.0033 (4)	0.0135 (5)	0.0001 (3)	−0.0038 (3)	0.0013 (4)	0.0160 (6)	0.0077 (3)	0.0030 (5)

(iii) contributions unrelated to motion, *e.g.* structural disorder.

Contributions of the first type are represented in terms of their vibrational frequencies and eigenvectors, the latter two are combined in the temperature-independent correction tensor ϵ, a symmetric second rank, mean-square displacement tensor, analogous to an ADP tensor.

NKA works in Cartesian space: a molecular coordinate system is generated based on the inertia tensor, which can be transformed to any user-specified molecular coordinate system. In the present case, the z axis is aligned with the threefold rotation axis and the x axis is taken parallel to the crystallographic a axis. NKA requires input of the full molecule in point-group symmetry 1 (C_1), therefore, the 32 (D_3) symmetric molecules of (1) and (2) were expanded using a locally written program, which also handles standard uncertainties properly (Parois, 2010).

Symmetry is re-introduced by a proper choice of the model. From group theory it is known that in point group 32 (D_3) libration around the z axis (L_z) and translation along the z axis (T_z) both transform as the irreducible representation A_2. Libration around the x and y axes (L_x, L_y) transform as E, as does translation along the x and y axes (T_x, T_y). Therefore, there are two non-degenerate and two pairs of degenerate (equal) normal modes. Each eigenvector has only two components, a librational and a translational one. Owing to eigenvector normalization, only one of the two components is independent. To stabilize the least-squares procedure, the eigenvectors belonging to the doubly degenerate eigenvalues were restrained to be aligned with the x and y axes of the coordinate system (owing to the degeneracy of the normal modes, any vector in the xy plane is a valid eigenvector).

Each different atom type, *i.e.* the Zn, Cu, N and C, was assigned an individual temperature-independent correction tensor ϵ with its own local coordinate system. For the C atoms, the local coordinate system has x along the C—N bond and y perpendicular to x in the C—C—N plane. For the N atoms, x points along the N—M bond, y is perpendicular to x in the N—M—N ligand plane. For all ϵ tensors, z completes a right-handed orthogonal system. The ϵ tensors of C and N have no symmetry restrictions. To maintain the molecular 32 (D_3) symmetry, the local coordinate systems for the different C and N atoms are related by the appropriate symmetry transformation. The local coordinate system of the metal atoms coincides with the molecular coordinate systems. The 32 (D_3) symmetry restrictions require that for these atoms $\epsilon_{11} = \epsilon_{22}$ and that $\epsilon_{12} = \epsilon_{13} = \epsilon_{23} = 0$. H atoms were included in the calculation of the inertia tensor, but not in the *NKA* least-squares refinement; $1/\sigma^2$ weights with σ values from *SHELXL* least-squares structure refinement were used. The total number of refinable parameters is 22 for each of the two compounds, the number of observed independent ADPs is 84 (six temperatures) for (1) and 70 (five temperatures) for (2). For comparison: in the rigid-body refinements (§4.2) the number of independent parameters was 36 for (1) and 30 for (2) (T_1, T_3, L_1, L_3, S_1 and S_3 at each temperature).

The results of the *NKA* analysis are summarized in Tables 4 and 5. The former summarizes the normal mode frequencies and their eigenvectors. The frequencies are in the expected range (< 100 cm^{-1}) and their magnitudes are consistent

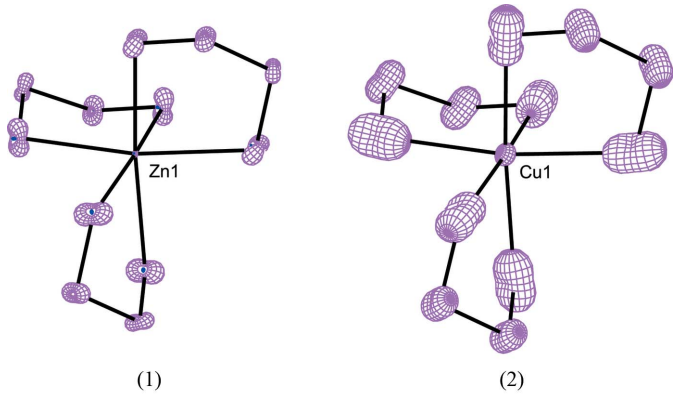

Figure 6
Root mean-square displacement surfaces for (1) (left) and (2) (right) showing scaled ϵ tensors calculated with *NKA* (Bürgi & Capelli, 2000). Scale is 3.00, light gray lines (red in the electronic online version) indicate positive r.m.s.d., dark gray lines (blue in the online version) negative r.m.s.d.

between (1) and (2). For both compounds the eigenvectors are either mostly translation or mostly libration, in agreement with the results from the TLS fits, which found the screw-coupling elements S_{ii} to be very small. The T and L tensor elements calculated from the normal modes are generally smaller than those found in the rigid-body analysis. The differences arise because the T and L tensors from normal mode analysis are entirely due to thermal motion, whereas those from rigid-body analyses include contributions from motion and disorder, as has been discussed in §4.2 (see Tables S3 and S4 of the supplementary material). Table 5 lists the ϵ tensors and their eigenvalues. For (1) the largest eigenvalues are $\lambda_3(\epsilon\mathrm{N})$ and $\lambda_1(\epsilon\mathrm{C})$. They correspond to displacements in directions that are approximately perpendicular to the N—Zn—N and N—C—C planes. $\lambda_3(\epsilon\mathrm{N})$ parametrizes the residual on N unaccounted for by the rigid-body analysis (Fig. 5). Note that the temperature-independent ϵ may contribute up to 50% to the ADPs at 140 K and as much as 25% at 290 K. As before, these residuals are too large to be interpreted in terms of intramolecular vibrations, but may be seen as an effect of ring puckering and intermolecular hydrogen-bonding disorder.

As is the case for ADPs, the eigenvalues of the ϵ tensors need to be positive to be physically meaningful (Bürgi & Capelli, 2000). However, $\lambda_1(\epsilon\mathrm{N})$ is significantly smaller than 0, whereas $\lambda_3(\epsilon\mathrm{Zn})$ and $\lambda_3(\epsilon\mathrm{C})$ equal 0 within their standard deviations (Table 5). The magnitudes of the remaining eigenvalues are typical of contributions from high-frequency normal modes.

A possible reason for the negative eigenvalues is anharmonicity in the thermal motion owing to thermal expansion of the unit cell (Bürgi *et al.*, 2000). In such cases, observed ADPs tend to be systematically larger than ADPs calculated from a harmonic model. To account for anharmonicity, a Grüneisen-type correction for the frequencies can be introduced into the model: $\nu = \nu_0(1 + \gamma_\mathrm{G})\Delta V(T)/V_\mathrm{min}$ with γ_G as the Grüneisen parameter and $V(T)$ the series expansion of the volume. A positive Grüneisen parameter reduces the frequencies of the normal modes with increasing unit-cell volume. In the case of (1) the ϵ tensors are still non-positive definite after the application of a Grüneisen correction and the agreement between calculated and measured ADPs does not improve. The failure of the Grüneisen correction in (1) may arise from the lack of data at very low temperatures. Such data are not accessible owing to the solid-solid phase transition (Lutz, 2010). The failure is not too surprising, however, given the linear dependence of the ADPs on temperature, *i.e.* their harmonic behaviour. The value of $\lambda_1(\epsilon N)$ is small, but appears significant at −0.0019 (3) Å^2. The uncertainty in dissecting the ADPs of (1) [and probably also of (2)] into contributions from thermal motion and disorder components may be of this order of magnitude, rather larger than indicated by the standard uncertainties.

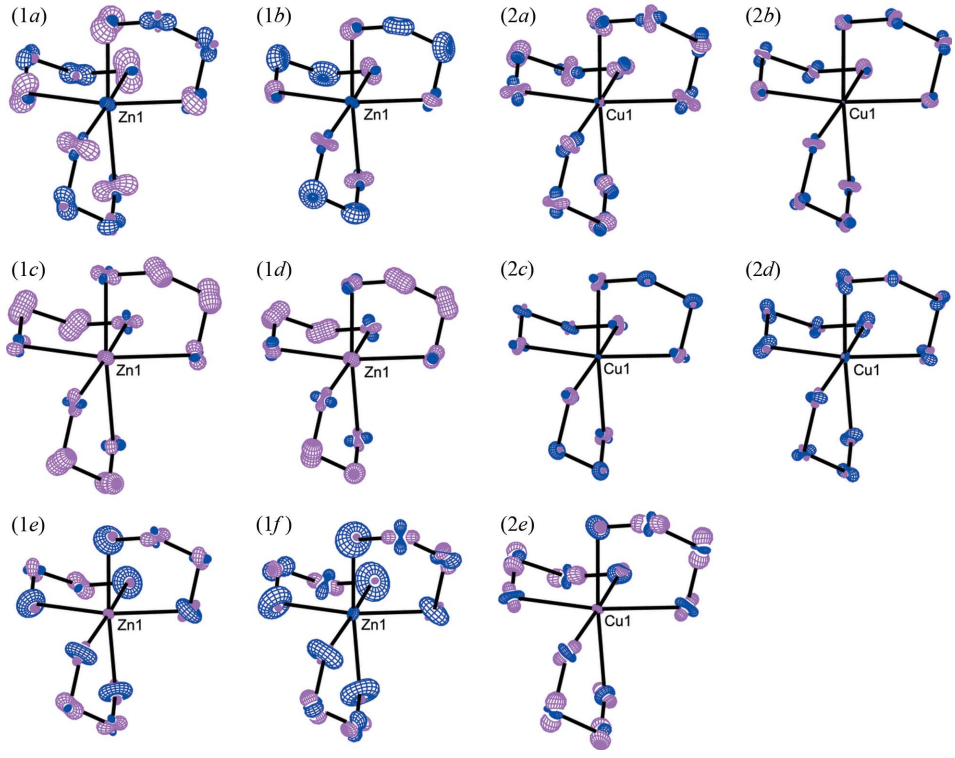

Figure 7
PEANUT plots $(U_\mathrm{obs} - U_\mathrm{calc})^{1/2}$ × scale (Hummel *et al.*, 1990) of (1) (left) at (1*a*) 140, (1*b*) 170, (1*c*) 200, (1*d*) 230, (1*e*) 260 and (1*f*) 290 K, and (2) (right) at (2*a*) 190, (2*b*) 210, (2*c*) 230, (2*d*) 250 and (2*e*) 270 K. The plots show the differences between the observed ADPs and those calculated from a normal mode model of motion with the program *NKA* (Bürgi & Capelli, 2000). The scale is 12.3, light gray lines (red in the electronic online version) indicate positive differences, dark gray lines (blue in the online version) negative differences.

All eigenvalues of the ϵ tensors in (2) are positive, several of them larger than values of 0.004–5 Å^2 expected to arise from intramolecular vibrations (Table 4). Their percentage contribution to the ADPs at 190 K is even larger than found for (1). The largest eigenvalue is $\lambda_3(\epsilon\mathrm{N})$, its eigenvector being nearly collinear with the N—Cu bond, again parametrizing what was a residual ADP on N in the rigid-body analyses (Fig. 5) and accounting for the disorder expected from the superposition of three Jahn–Teller distorted complexes. The eigenvector corresponding to $\lambda_2(\epsilon\mathrm{N})$ is oriented approximately perpendicular to the N—Cu—N plane. This finding is consistent with the corresponding *NKA* result for (1). Fig. 6 compares plots of the ϵ tensors of (1) and (2). Both plots show similar features, albeit of different magnitude. They are assigned to ring-puckering disorder of the C and

N atoms, and to unbalanced intermolecular hydrogen bonding. The two plots differ in that (2) shows the effects of the Jahn–Teller distortion which are absent in (1).

The ADPs calculated from the *NKA* models show much better agreement with the observed data than those from the rigid-body models: the R values[3] for (1) and (2) are 0.027 and 0013, the goodness-of-fit[4] values are 1.08 and 0.58 [calculated based on 1 (C_1) symmetry]. *PEANUT* plots of the residuals, representing the unexplained parts of the ADPs, show no easily interpretable features and look fairly uncorrelated between temperatures (Fig. 7). This indicates that the NKA model fully accounts for the ADPs measured over the temperature range 80–150 K, in terms of the temperature-dependent thermal motion contributions on one hand and the effects of unresolved atomic positional disorder on the other.

5. The degree of Jahn–Teller distortion of (2) and some conclusions

One way of quantifying a Jahn–Teller distortion is in terms of the so-called Jahn–Teller radius $R_{\rm JT}$, which describes a Mexican hat potential that connects the three possible tetragonally elongated structures of an octahedral Cu^{II} complex across low-energy barriers along its rim. The radius can be obtained from the bond distances of a statically distorted Cu^{II} complex as

$$R_{\rm JT} = \left\{ \sum_{i=1}^{6} (d_i - \langle d \rangle)^2 \right\}^{1/2}. \qquad (1)$$

Ammeter *et al.* (1979) have shown that for disordered CuN_6 complexes like (2), with six equal Cu—N distances, the quantity $R_{\rm JT}$ may be obtained from Hirshfeld differences according to

$$R_{\rm JT} = \left\{ \sum_{i=1}^{6} \Big(U_z(\mathrm{N}_i) - U_z(\mathrm{Cu}) \Big) - \Big(U_z(\mathrm{N}_i) - U_z(\mathrm{Zn}) \Big) \right\}^{1/2}. \qquad (2)$$

The term involving the Zn complex corrects for the contribution of the M—N stretching vibrations to the ADPs not related to Jahn–Teller distortion (see §4.1). If no data for an isostructural Ni or Zn complex are available, it is preferable to resort to structures of accurately determined, closely related complexes rather than to neglect the correction and thus to compromise the accuracy of $R_{\rm JT}$. The radii $R_{\rm JT}(d_i)$ from the statically distorted low-temperature structure are 0.382 and 0.384 Å (two molecules in the asymmetric unit; Lutz, 2010). They may be compared with the independently determined value $R_{\rm JT}(\Delta U_z)$, which is 0.389 Å; a good agreement.

The results presented here illustrate that a normal-mode analysis identifies the low-frequency motions which are responsible for the temperature-dependence of the ADPs and separates them from the largely temperature-independent disorder contributions with a reasonable degree of reliability. What is needed are ADPs measured over a range of temperature that is sufficiently large and sufficiently close to T = 0 K. It is recalled that such a separation is not possible with conventional TLS analysis. In the present case we have considered disorder originating from Jahn–Teller distortions, from hydrogen bonding not satisfying the average crystallographic 32 (D_3) symmetry and from the flexibility/adaptability of the half-chair conformation of the five-membered rings. The combination of motion and disorder accounts for more than 97% of the observed ADPs of (1) and (2).

The two complexes (1) and (2) show phase transitions during cooling, accompanied by a lowering of symmetry. The transition temperatures are very different. For (2) a transition between $P\bar{3}1c$ and $P\bar{1}$ (Lutz, 2010) occurs at 180 K (Bertini *et al.*, 1977). For (1) the transition temperature has not been determined accurately: at 140 K the $P\bar{3}1c$ phase has been observed, at 110 K the low-temperature $P\bar{3}$ phase (Lutz, 2010). The Ni complex which is isostructural with (1) undergoes the same symmetry change during its phase transition (Jameson *et al.*, 1982). Compound (1) and the Ni complex are both Jahn–Teller inactive, but the transition temperature of 180 K for the Ni complex is equal to that of the Jahn–Teller distorted (2) and more than 40 K higher than for (1). These differences in transition temperatures seem to depend on subtle differences in the structures and dynamics of the corresponding crystal structures and cannot solely be attributed to the presence or absence of Jahn–Teller motion.

[3] $wR_2 = [\sum w(U_{\rm obs} - U_{\rm calc})^2 / \sum w U_{\rm obs}^2]^{1/2}$ with $w = 1/\sigma^2$.
[4] GooF $= \sum (wU_{\rm obs} - wU_{\rm calc})^2 / (n_{\rm obs} - n_{\rm par})$ with $w = 1/\sigma^2$.

References

Ammeter, J., Bürgi, H. B., Gamp, E., Meyer-Sandrin, V. & Jensen, W. P. (1979). *Inorg. Chem.* **18**, 733–750.
Bertini, I., Dapporto, P., Gatteschi, D. & Scozzafava, A. (1979). *J. Chem. Soc. Dalton Trans.* pp. 1409–1414.
Bertini, I., Gatteschi, D. & Scozzafava, A. (1977). *Inorg. Chem.* **16**, 1973–1976.
Bürgi, H. B. & Capelli, S. C. (2000). *Acta Cryst.* A**56**, 403–412.
Bürgi, H. B. & Capelli, S. C. (2003). *Helv. Chim. Acta*, **86**, 1625–1640.
Bürgi, H. B., Capelli, S. C. & Birkedal, H. (2000). *Acta Cryst.* A**56**, 425–435.
Capelli, S. C., Förtsch, M. & Bürgi, H. B. (2000). *Acta Cryst.* A**56**, 413–424.
Caughlan, C. N., Mazhar-ul-Haque & Emerson, K. (1970). *Inorg. Chem.* **9**, 2421–2424.
Cola, M., Giuseppetti, G. & Mazzi, F. (1962). *Atti. Accad. Sci. Torino, Classe Sci. Fis., Mat. Nat.* **96**, 381–408.
Cullen, D. L. & Lingafelter, E. C. (1970). *Inorg. Chem.* **9**, 1858–1864.
Daniels, L. M., Murillo, C. A. & Rodríguez, K. G. (1995). *Inorg. Chim. Acta*, **229**, 27–32.
Dittrich, B., McKinnon, J. J. & Warren, J. E. (2008). *Acta Cryst.* B**64**, 750–759.
Falvello, L. R. (1997). *J. Chem. Soc. Dalton Trans.* pp. 4463–4475.
Halcrow, M. E. (2003). *Dalton Trans.* pp. 4375–4384.
Hanson, R. M. (2010). *J. Appl. Cryst.* **43**, 1250–1260, http://jmol.sourceforge.net/.
Hirshfeld, F. L. (1976). *Acta Cryst.* A**32**, 239–244.
Hummel, W., Hauser, J. & Bürgi, H. B. (1990). *J. Mol. Graph.* **8**, 214–220.
Jameson, G. B., Schneider, R., Dubler, E. & Oswald, H. R. (1982). *Acta Cryst.* B**38**, 3016–3020.

Lutz, M. (2010). *Acta Cryst.* C**66**, m330–m335.
Neverov, V., Mazus, M., Biyushkin, V. & Malinowskii, T. (1990). *Kristallografiya*, **35**, 1281–1283.
Nonius (1999). *COLLECT*. Nonius BV, Delft, The Netherlands.
Parois, P. (2010). Unpublished.
Schomaker, V. & Trueblood, K. N. (1998). *Acta Cryst.* B**54**, 507–514.
Schreurs, A. M. M. (2005). *PEAKREF*. Utrecht University, The Netherlands.
Schreurs, A. M. M., Xian, X. & Kroon-Batenburg, L. M. J. (2010). *J. Appl. Cryst.* **43**, 70–82.
Sheldrick, G. M. (2008*a*). *Acta Cryst.* A**64**, 112–122.
Sheldrick, G. M. (2008*b*). *SADABS*. University of Göttingen, Germany.
Spek, A. L. (2009). *Acta Cryst.* D**65**, 148–155.
Yotnoi, B., Seeharaj, A., Chimupala, Y. & Rujiwatra, A. (2010). *Acta Cryst.* E**66**, m628.